

6. RELATIONS BETWEEN TEXTURAL CHARACTERISTICS AND PHYSICAL PROPERTIES OF SEDIMENTS IN NORTHWESTERN CASCADIA BASIN¹

Amanda Cavin,² Michael Underwood,² Andrew Fisher,³ and Aaron Johnston-Karas³

INTRODUCTION

Sedimentary deposits of Cascadia Basin lap onto the Juan de Fuca Ridge to within 20 km of the spreading axis (Davis and Currie, 1993). Collectively, these interbeds of hemipelagic mud, mud turbidites, silt turbidites, sand turbidites, and debris-flow deposits act as a relatively low-permeability barrier that inhibits the hydrothermal connection between underlying igneous crust and the overlying reservoir of ocean water. The primary purpose of Leg 168 of the Ocean Drilling Program (ODP) was to explore the causes and consequences of ridge-flank hydrothermal circulation (Shipboard Scientific Party, 1997c). One important aspect of this overall goal was to determine how changes in thickness of the sediment cover affect heat flow, fluid flow, fluid composition, and chemical alteration of the igneous crust. Fluid circulation through the sediment is influenced by a variety of textural parameters and intrinsic physical properties. Physical properties of sediments usually change in a predictable way with increasing depth and mechanical compaction, but different lithologies display different compaction gradients.

During Leg 168, 10 drill sites were organized into three transects. The Hydrothermal Transition Transect is located closest to the ridge crest and includes Sites 1023, 1024, and 1025 (Fig. 1). The total thickness of sediment above igneous basement ranges from 192.8 m at Site 1023 to 97.5 m at Site 1025. The Rough Basement Transect is located ~100 km from the ridge crest and includes Sites 1026 and 1027. Sediment thickness there ranges from 228.9 m above a basement high (Site 1026) to 606.2 m above an adjacent basement low (Site 1027). The Buried Basement Transect begins 40 km from the ridge crest, above a basement high, and extends approximately 35 km to the east. Sites 1030 and 1031 are located above the basement high and contain less than 45 m of sediment (Fig. 1). Sedimentary successions at Sites 1028 and 1029 reach thicknesses of 132.5 m and 220.1 m, respectively. Site 1032 was used primarily as a logging site and was not sampled as part of this study.

Shipboard scientists subdivided the sedimentary succession throughout the study area into three principal lithofacies units and sub-units (Fig. 1). In general, these sequences coarsen and thicken upward from a basal interval of hemipelagic mud through a unit of mud and silt turbidites into a unit of mud, silt turbidites, sand turbidites, and debris-flow deposits. The sediment index properties (bulk density, water content, porosity, and void ratio) were measured aboard the *JOIDES Resolution* (Shipboard Scientific Party, 1997b, 1997d, 1997a). Shore-based work was devoted to accurate measurements of grain-size parameters. To allow for valid cross-correlation, the samples analyzed for grain-size distributions were taken from core intervals immediately

adjacent to those of the physical properties specimens. The main purposes of this report are to show how the grain size and physical properties data are interrelated, and to determine how lithology might affect hydrologic properties of the sedimentary cover.

LABORATORY METHODS

The chores of sample preparation were divided equally between labs at the University of Missouri and University of California, Santa Cruz. Because of subtle differences in procedure, several samples were split and prepared in both labs to test for reproducibility (Table 1). The first step in sample preparation was to remove pore water by freeze drying. Dried samples (typically 10–20 g) were stored in a desiccator to prevent moisture from being absorbed, and the dry weights were recorded. The samples then were transferred to 600-mL beakers and immersed in hydrogen peroxide to digest organic matter. After at least 24 hr of digestion and periodic stirring, 250 mL of sodium hexametaphosphate (Calgon) solution (4 g per 1000 mL deionized water) were added to each beaker to assist disaggregation and prevent clay flocculation. After sitting in Calgon solution for at least 12 hr, the beakers were immersed in an ultrasonic bath for 5–10 min to enhance disaggregation further. Suspensions were washed through a 63- μ m screen to separate sand-sized grains from silt and clay. Each sand portion was collected, dried in an oven, and weighed. Each fraction <63 μ m was collected in a large evaporating dish and transferred to a 500-mL Nalgene bottle. A centrifuge was used to reduce water volumes by roughly one-half (at 8000 rpm for 20 min), and sediment was washed out of the centrifuge tubes with Calgon solution. The concentrated suspensions were stored in 125-mL Nalgene bottles until analysis.

The SediGraph 5000ET grain-size analyzer measures the attenuation of X-rays by particles that are suspended in a solution (Jones et al., 1988). Comparisons among the results of SediGraph analysis and results using other instruments and techniques have been described by Stein (1985), Singer et al. (1988), and Camerlenghi et al. (1995). The SediGraph determines the concentration of particles remaining at decreasing depths within a suspension as a function of time. The principle of Stoke's Law of Settling is used to convert vertical profiles of suspension density to weight percentages of grain size. Before analysis, sample bottles were shaken vigorously for several minutes to resuspend and disaggregate the sediment particles. Approximately 60 mL of suspension were poured into the SediGraph chamber. In some cases, the concentrations had to be adjusted to fall within an acceptable range of kilocounts/s. Rigorous characterization of size fractions less than 0.5 μ m requires settling times that are prohibitively long; in addition, absolute size data in the submicron range from the SediGraph are of questionable reliability (Singer et al., 1988). In most cases, measurements to 0.5 μ m took ~10 min and allowed us to characterize the size distribution to between 30% and 40% cumulative mass finer.

Data output from SediGraph software includes a table and cumulative curve of mass percentages finer over a range of sizes from 63

¹Fisher, A., Davis, E.E., and Escutia, C. (Eds.), 2000. *Proc. ODP, Sci. Results*, 168: College Station TX (Ocean Drilling Program).

²Department of Geological Sciences, University of Missouri, Columbia MO 65211, USA. Correspondence author: UnderwoodM@missouri.edu

³Earth Sciences Department, University of California, Santa Cruz, Santa Cruz CA 95064, USA.

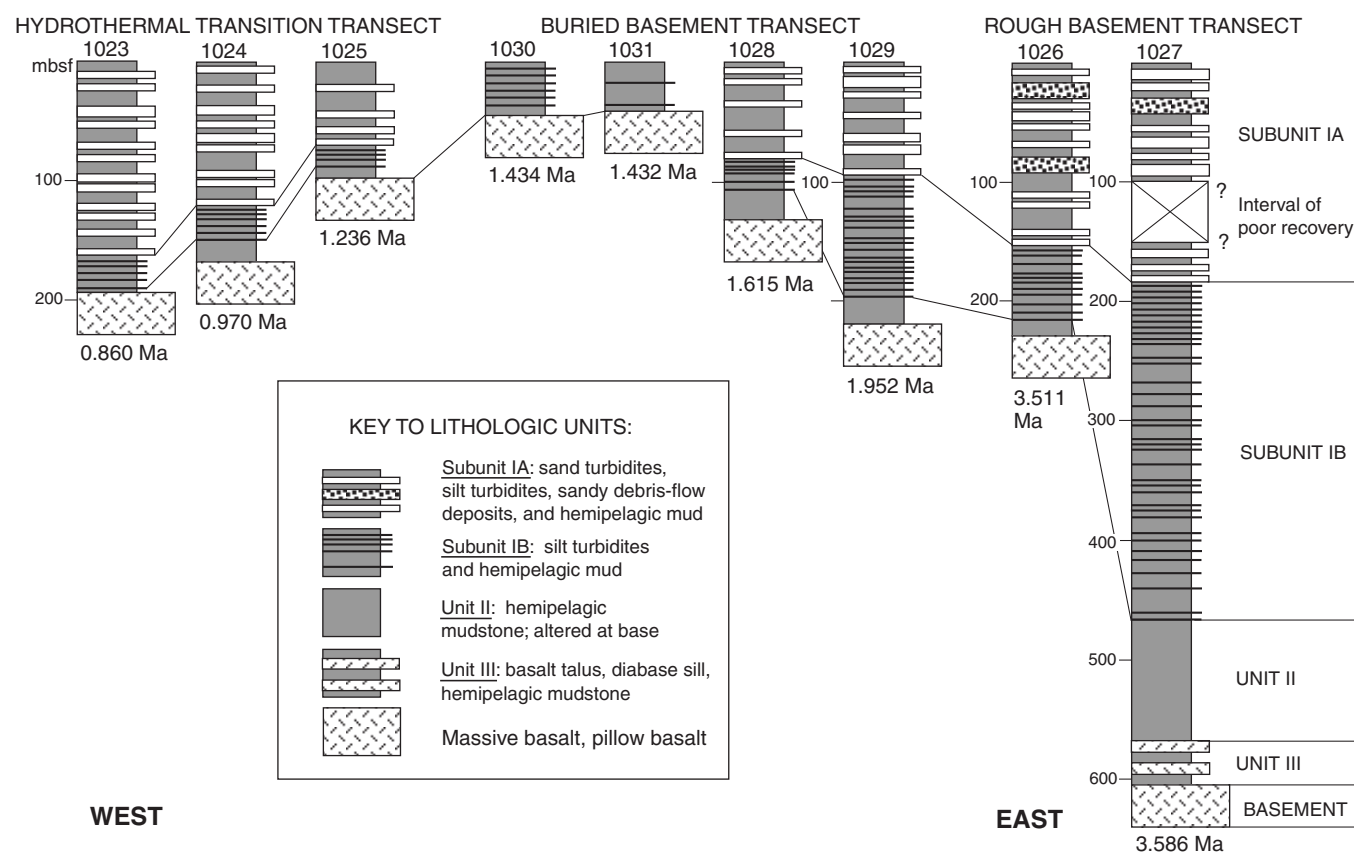


Figure 1. Lithostratigraphy of the ODP Leg 168 drill sites. Ages of basaltic basement (from Shipboard Scientific Party, 1997c) are provided in Ma.

Table 1. Grain-size statistics.

Core, section	Interval (cm)	Depth (mbsf)	75th percentile (µm)	50th percentile (µm)	25th percentile (µm)	Mean diameter (µm)	Sorting coefficient	Geometric skewness	Sand (wt%)	Silt (wt%)	Clay (wt%)
168-1023A-											
1H-2	73-76	2.23	8.2	1.9	0.4	3.5	4.8	0.89	0.3	38.6	61.1
1H-4	72-75	5.22		Unreliable SediGraph data							
2H-1	85-87	10.15	5.0	1.6	0.4	2.3	3.5	0.88	4.0	28.8	67.2
2H-5	135-137	16.65	11.4	4.5	1.1	5.7	3.2	0.79	1.0	51.8	47.2
3H-1	129-132	20.09	2.9	0.9	0.3	1.4	3.2	1.00	1.6	17.8	80.6
3H-2	42-43	20.74	3.9	1.2	0.4	1.8	3.1	1.04	5.2	23.1	71.7
4H-3	108-110	32.38		Unreliable SediGraph data							
4H-6	58-60	36.38	34.3	22.7	10.4	22.5	1.8	0.83	32.5	54.0	13.5
5H-2	41-43	39.71	20.1	12.3	4.3	12.2	2.2	0.76	7.0	70.2	22.8
5H-4	110-112	43.40		Unreliable SediGraph data							
5H-5	105-107	44.85	33.7	21.5	3.1	19.4	3.3	0.48	50.0	36.5	13.6

This is a sample of the table that appears on the volume CD-ROM.

to 0.5 µm, plus values of the median diameter (d_{50}) and cumulative mass finer than 4 µm (clay fraction). Weight percentages of sand were calculated by dividing the weight of the sediment coarser than 63 µm (from sieving) by the total dry weight that was measured after freeze drying. We regarded the total dry weight minus the sand weight as equal to the weight of silt + clay, even though this difference includes an error equal to the weight of digested organic matter. The weight percentages of silt and clay fractions were calculated by multiplying the weight of silt + clay by the cumulative percents >4 µm and <4 µm, respectively.

Digital data were downloaded to a graphics application and replotted to extrapolate the cumulative curve (by linear extension) beyond the 75th percentile and to digitize the diameter values (in micrometers) at the 25th and 75th percentiles (d_{25} and d_{75}). These quartile measures were used to calculate three statistics for the silt + clay fraction: mean (M_g), geometric sorting coefficient (S_o), and geomet-

ric skewness (S_{kg}), following Krumbein (1936). The relevant equations are

$$M_g = [d_{25} + d_{50} + d_{75}] \div 3,$$

$$S_o = [d_{75} \div d_{25}]^{0.5}, \text{ and}$$

$$S_{kg} = [(d_{75})(d_{25}) \div (d_{50})^2]^{0.5}.$$

A symmetrical distribution of particle sizes results in a geometric skewness equal to unity. Sorting coefficients less than 2.5 are indicative of well-sorted samples; coefficients greater than 4.5 are indicative of poor sorting. We emphasize here that these statistics pertain only to the size fraction analyzed by SediGraph (<63 µm), not the total grain-size distribution.

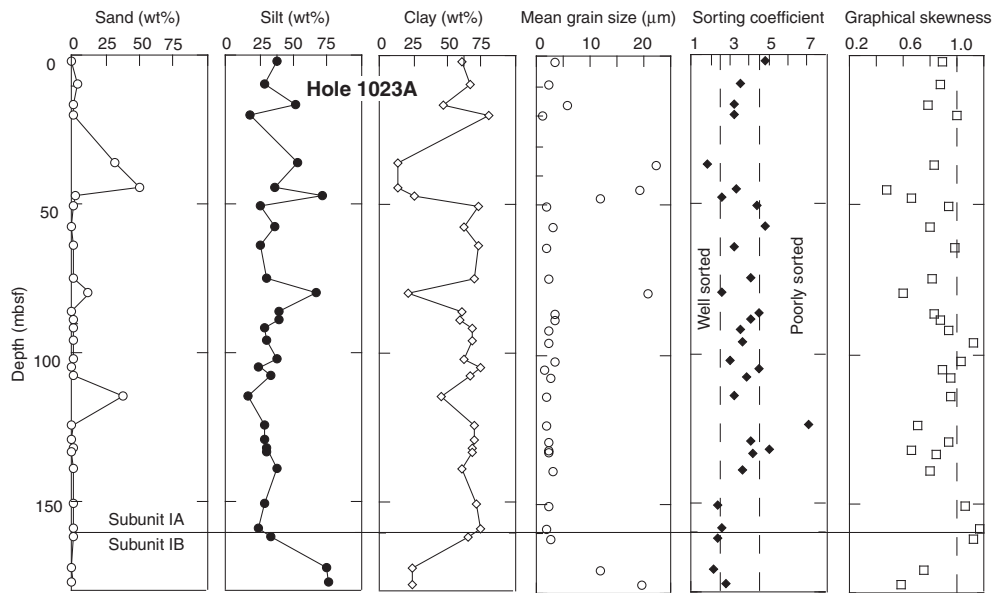


Figure 2. Depth variations in grain-size statistics for samples from Site 1023. Values of mean grain size, sorting coefficient, and graphical skewness are based on quartile measures (Krumbein, 1936) and apply only to the size fractions (<63 μm) that were analyzed by SediGraph.

RESULTS

The results of grain-size analyses, including duplicate runs, are listed on Table 1. In a relatively small number of instances, cumulative curves displayed erratic geometries because of low suspension concentrations or sharp deflections in slope that we regarded as spurious instrument behavior. These samples are identified in Table 1, but their results are not included. All of the reliable data are plotted vs. sample depth at each site. Regression plots also show either weight-percentage clay or mean grain size vs. the sediment index properties (water content, porosity, void ratio, and bulk density). Figures 2 and 3 illustrate results for Site 1023. Similar graphics for the other sites are included in Figures 6–21.

Percentages of sand, silt, and clay do not show any consistent trends as a function of depth at any site. Similarly, there seems to be very little change in the texture of hemipelagic mud from Subunit IA to Subunit IB to Unit II. Sampling of sandy and silty turbidite layers during shipboard measurements was not done in a systematic manner, so the specific depths where we plot excursions toward coarser grain sizes are not representative of the actual turbidite distribution in the cores. In addition, no attempt was made during sampling to distinguish between hemipelagic mud and turbidite mud. Sand-sized grains constitute less than 1% of most muds, and the clay content is typically between 60% and 85% (Fig. 2). Most of these silty clays are moderately well sorted, and skewness values are typically between 1.0 and 0.7. In general, mean grain size for the silt + clay fraction of the muds ranges from 1 to 4 μm , whereas mean grain size for the silt + clay fraction of sandy turbidites is typically between 10 and 20 μm .

Combining all of the data from all of the cores shows a clear segregation between the mud and sand/silt lithologies (Fig. 4). Regression plots show considerable sensitivity of index properties to the content of clay-sized particles (Fig. 3). Water content, porosity, and void ratio generally increase with increasing clay content, whereas bulk density tends to decrease. Correlation coefficients for the linear regressions range from 0.03 to 0.79 (Figs. 3, 7, 9, 11, 13, 15, 17, 19, and 21). For most of the data populations, these coefficients indicate that the correlations between clay content and index properties are statistically significant at a confidence level of 95%, but it is also clear that other factors are involved. Superimposed upon the effects of grain size are the mechanical changes that occur with depth-dependent compaction. The compaction gradients for muds differ sig-

nificantly from those of silt and sand turbidites (Shipboard Scientific Party, 1997b, 1997d, 1997a). Most of the borehole successions display systematic effects of compaction within the mud component, but dewatering is most pronounced at Site 1027, where sediment thickness reaches 600 m. In contrast, the initial porosities of turbidites tend to be significantly lower, and there is less dewatering, if any, with depth.

At Sites 1030 and 1031, mud porosities remain high (65%–80%) throughout the relatively thin sediment cover (<45 m). The pore-water profiles at both sites also show clear evidence of upward fluid flow (Shipboard Scientific Party, 1997a). The textural characteristics of these muds appear to be no different than those of hemipelagic deposits at the other sites (Figs. 18 and 20). As discussed below, their somewhat unusual physical properties probably persist because the overburden at Sites 1030 and 1031 is too thin to collapse the grain fabric inherited from suspension fallout.

DISCUSSION AND CONCLUSIONS

The motivation for analyzing grain-size distributions in such a comprehensive manner was to determine whether or not the character of the overlying sediment column exerts any influence on the transfer of hydrothermal fluids, either into or out of the underlying igneous basement. Because fluid migration is sensitive to the physical properties of sediments, one indirect way to address the link from lithology to hydrology is to determine whether or not physical properties change as a function of grain size. For the most part, our study quantified two obvious relations: hemipelagic and/or turbidite mud is finer grained than turbidite sand and silt, and physical properties within the stratigraphic column change in response to both initial sediment texture and depth of burial.

Shipboard measurements showed that a large range exists in the physical properties of sediments, particularly within the upper 100–150 m of the stratigraphic successions. Porosity values, for example, range from 80% to 30% (Fig. 5A). Much of this scatter can be attributed to the interlayering of several lithologies within lithostratigraphic Subunits IA and IB. When data from the coarser samples are segregated from the porosity values of mud samples, two compaction trends emerge (Fig. 5B). All but two porosity values for sandy samples fall between 55% and 35%, but there is no systematic

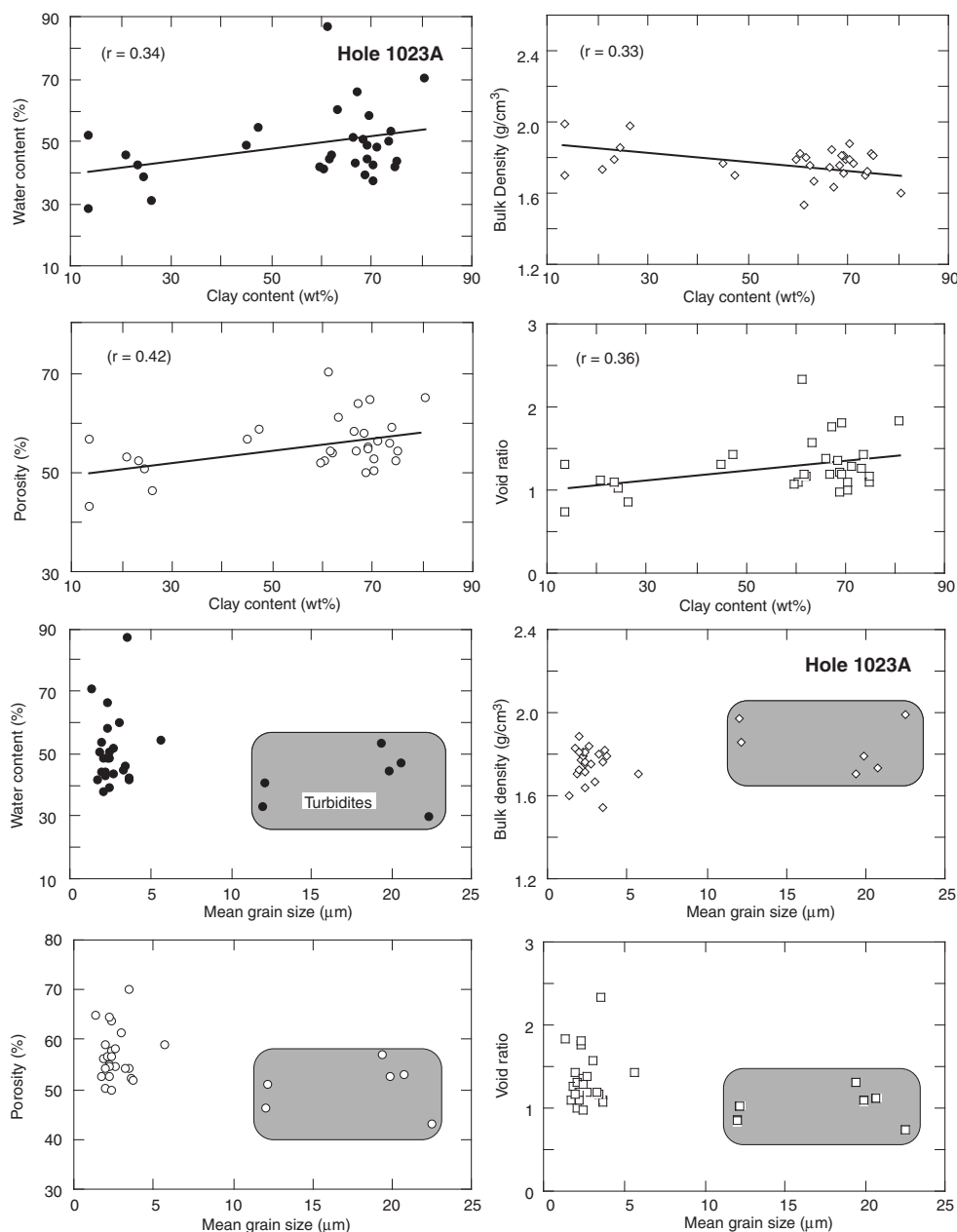


Figure 3. Cross plots of weight-percent clay (<4- μm size fraction) and mean grain size (μm) vs. index properties of sediment (porosity, void ratio, water content, and bulk density) as determined by shipboard measurements of samples from Site 1023 (Shipboard Scientific Party, 1997b). Values of mean grain size are based on quartile measures (Krumbein, 1936) and apply only to the size fractions (<63 μm) that were analyzed by SediGraph. Note the separation of fields for turbidites and hemipelagic muds. Values of r are correlation coefficients for linear regression.

change in sand porosity over a depth range of 0–120 mbsf. Conversely, mud porosity near the seafloor is greater than 70%; values drop to ~40% at depths below 500 mbsf. Data from the mud samples fit a compaction curve (of the form $n = az^b$) to depths of ~200 mbsf. Below 200 mbsf, a linear compaction trend provides a better fit to the data (Fig. 5A). Separation between the sand-layer data and the mud compaction trend is pronounced within the upper 40 m of the sediment column (Fig. 5C). At depths greater than 50 mbsf, overlap begins to occur between the mud compaction gradient and the porosity field for sand (Fig. 5B).

Giambalvo et al. (2000) carefully examined samples that were collected for consolidation tests and were able to discriminate between hemipelagic and turbidite muds. Initial porosity values (i.e., prior to consolidation tests) for the hemipelagic specimens are signif-

icantly higher than initial porosity values for turbidite muds. Although their grain-size characteristics are similar, the hemipelagic muds contain more foraminifers, and scanning electron microscopy (SEM) showed that their grain fabrics are random to subvertical. Random grain orientations probably result from deposition as fecal pellets and/or flocculated aggregates. In contrast, the turbidite muds contain few, if any, foraminifers, and their grain fabrics show systematic bed-parallel alignment of phyllosilicates (Giambalvo et al., 2000). X-ray diffraction analyses did not reveal differences in mineralogy between the two types of mud (Underwood and Hoke, Chap. 5, this volume). Interbedding between these two types of mud, with similar texture and mineralogy but contrasting initial grain fabrics, helps explain why there is so much scatter in mud porosity values within the upper 150 m of sediment (Fig. 5B).

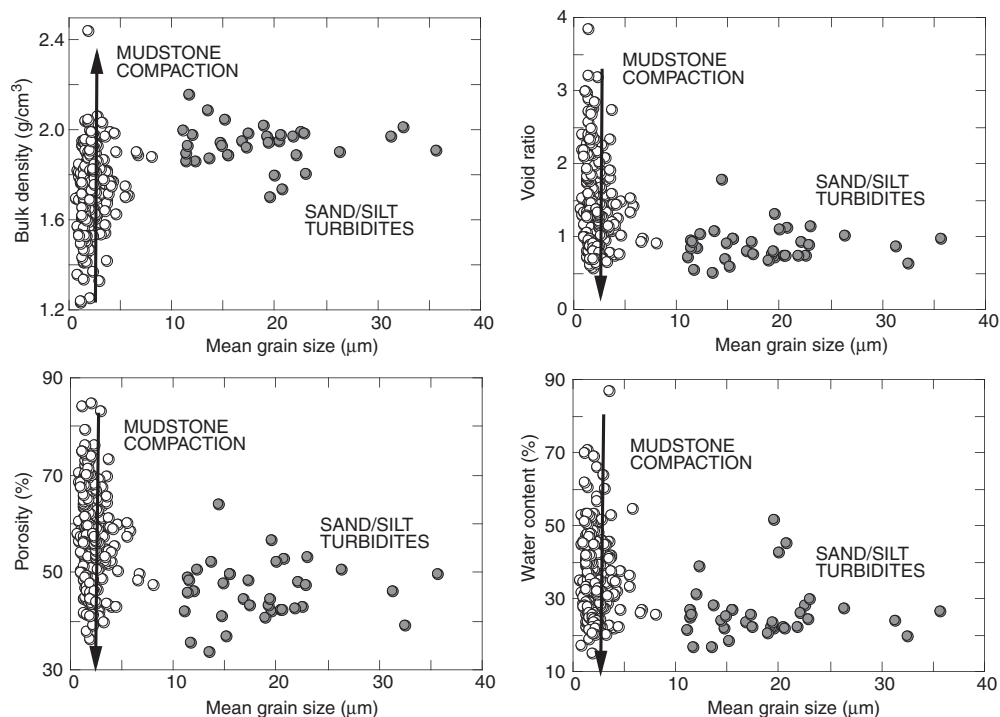


Figure 4. Cross plots of mean grain size (μm) vs. index properties of sediment (bulk density, porosity, void ratio, and water content) as determined by shipboard measurements of samples from all sites cored during Leg 168 (Shipboard Scientific Party, 1997b, 1997d, 1997a). Values of mean grain size are based on quartile measures (Krumbein, 1936) and apply only to the size fractions ($<63 \mu\text{m}$) that were analyzed by SediGraph. Note the separation of compaction responses for turbidites and hemipelagic muds.

One of the more intriguing phenomena to address during Leg 168 involves the transformation from a hydrologically open basement to a sealed basement. The early-stage sedimentary carapace of highly porous and permeable mud is gradually transformed to a thicker section of sediment that contains a more highly compacted and relatively impermeable seal at its base. With the exception of Site 1027, which includes a basal unit of basaltic sills, breccia, and carbonate-rich mud, the lithology resting above igneous basement is hemipelagic mud (Unit II). Once this fine-grained material compacts sufficiently, the basement becomes sealed, but exactly when this happens remains uncertain. At Sites 1030 and 1031, upflow of fluids through the sediment cover was inferred from pore-water profiles of conservative elements, and the estimated rate of upflow is $\sim 2 \text{ mm/yr}$ (Shipboard Scientific Party, 1997a). Evidently, the overburden at Sites 1030 and 1031 is too thin ($<45 \text{ m}$) to collapse the pore fabric of the basal mud unit.

Giambalvo et al. (2000) showed that sediments from the Site 1030/1031 seepage localities are overconsolidated; underconsolidated conditions might be expected if fluid pressures were significantly greater than hydrostatic. Instead, fluid overpressures appear to be $\leq 5 \text{ kPa}$ at the basement/sediment interface (Giambalvo et al., 2000). Because of their random grain fabrics, porosities for hemipelagic muds from the upflow sites are consistently higher when compared to undifferentiated mud (turbidite and hemipelagic) from comparable depths ($<42 \text{ mbsf}$) at sites of no flow (Fig. 5D). The average difference in porosity between the two groups of shallow mud samples is $\sim 7\%$. Those contrasts in porosity translate into $10\times$ differences in permeability; in addition, modeling indicates that the hemipelagic mud of Unit II could sustain geochemically detectable flow ($>0.1 \text{ mm/yr}$) up to burial depths of 150 m , assuming an overpressure of 5 kPa (Giambalvo et al., 2000). Thus, the overlying turbidite section (Subunits IA and IB) is entirely responsible for increasing the lithostatic load enough to compact the basal hemipelagic mud, but the textural characteristics of the turbidites are probably not important in the process of sealing the basement.

ACKNOWLEDGMENTS

We thank the crew, technicians, and fellow scientists who sailed on *JOIDES Resolution* during Leg 168 for their help with sample acquisition. Shorebased work was supported by USSSP Grants 168-F000421, 168-F000502, and 168-F000503. Brandon Gomer assisted with sample preparation. Earl Davis and Bill Busch provided helpful reviews of the manuscript.

REFERENCES

- Camerlenghi, A., Lucchi, R.G., and Rothwell, R.G., 1995. Grain-size analysis and distribution in Cascadia Margin sediments, northeastern Pacific. In Carson, B., Westbrook, G.K., Musgrave, R.J., and Suess, E. (Eds.), *Proc. ODP, Sci. Results*, 146 (Pt 1): College Station, TX (Ocean Drilling Program), 3–31.
- Davis, E.E., and Currie, R.G., 1993. Geophysical observations of the northern Juan de Fuca Ridge system: lessons in sea-floor spreading. *Can. J. Earth Sci.*, 30:278–300.
- Giambalvo, E.R., Fisher, A.T., Martin, J.T., Darty, L., and Lowell, R.P., 2000. Origin of elevated sediment permeability in a hydrothermal seepage zone, eastern flank of the Juan de Fuca Ridge, and implications for transport of fluid and heat. *J. Geophys. Res.* 105:897–912.
- Jones, K.P.N., McCave, I.N., and Patel, P.D., 1988. A computer-interfaced SediGraph for modal size analysis of fine-grained sediment. *Sedimentology*, 35:163–172.
- Krumbein, W.C., 1936. The use of quartile measures in describing and comparing sediments. *Am. J. Sci.*, 32:98–111.
- Shipboard Scientific Party, 1997a. Buried basement transect (Sites 1028, 1029, 1030, 1031, and 1032). In Davis, E.E., Fisher, A.T., Firth, J.V., et al., *Proc. ODP, Init. Repts.*, 168: College Station, TX (Ocean Drilling Program), 161–212.
- , 1997b. Hydrothermal transition transect (Sites 1023, 1024, and 1025). In Davis, E.E., Fisher, A.T., Firth, J.V., et al., *Proc. ODP, Init. Repts.*, 168: College Station, TX (Ocean Drilling Program), 49–100.
- , 1997c. Introduction and summary: hydrothermal circulation in the oceanic crust and its consequences on the eastern flank of the Juan de

Fuca Ridge. In Davis, E.E., Fisher, A.T., Firth, J.V., et al., *Proc. ODP, Init. Repts.*, 168: College Station, TX (Ocean Drilling Program), 7–21.

———, 1997d. Rough basement transect (Sites 1026 and 1027). In Davis, E.E., Fisher, A.T., Firth, J.V., et al., *Proc. ODP, Init. Repts.*, 168: College Station, TX (Ocean Drilling Program), 101–160.

Singer, J.K., Anderson, J.B., Ledbetter, M.T., McCave, I.N., Jones, K.P.N., and Wright, R., 1988. An assessment of analytical techniques for the size analysis of fine-grained sediments. *J. Sediment. Petrol.*, 58:534–543.

Stein, R., 1985. Rapid grain-size analyses of clay and silt fraction by Sedi-graph 5000D: comparison with Coulter Counter and Atterberg methods. *J. Sediment. Petrol.*, 55:590–615.

Date of initial receipt: 10 December 1998

Date of acceptance: 20 May 1999

Ms 168SR-013

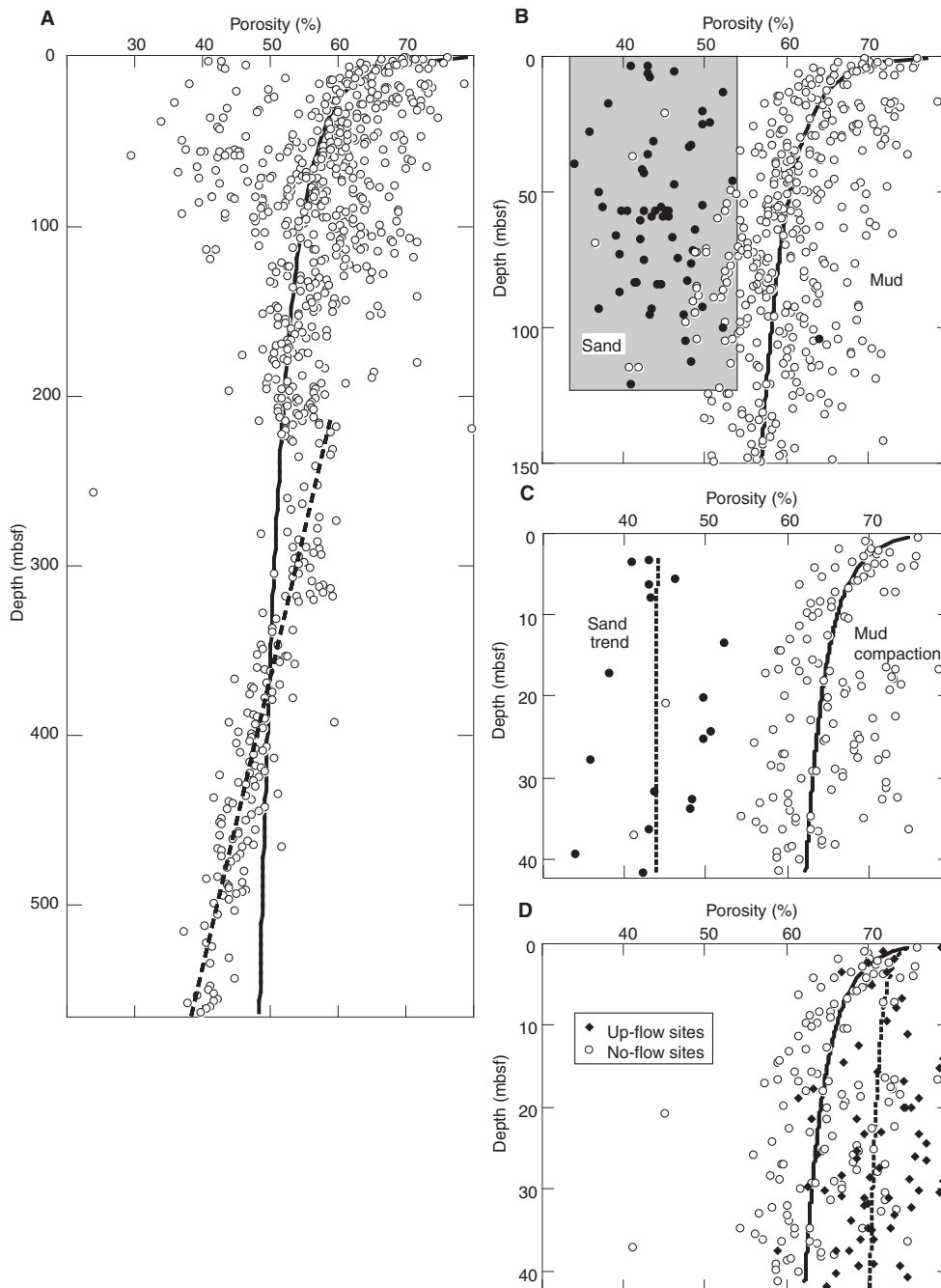


Figure 5. Depth profiles of sediment porosity as determined by shipboard measurements of samples from all sites cored during Leg 168 (Shipboard Scientific Party, 1997b, 1997d, 1997a). **A.** Complete compilation of data from no-flow sites (Sites 1023–1029), without segregation by lithology. A single compaction curve follows the form $n = az^b$. Note the shift to a linear compaction gradient at ~200 mbsf. **B.** Comparison of porosity trends for sand and mud lithologies within the upper 150 m at the no-flow sites. Turbidite sands become increasingly sparse below 120 mbsf. **C.** Comparison of porosity trends for sand and mud lithologies within the upper 42 m at the upflow sites (Sites 1030 and 1031) vs. the no-flow sites. The upflow sites contain mostly hemipelagic mud, whereas the no-flow sites at the same depths contain both hemipelagic and turbidite mud. Compaction curves for the two data sets show a shift of ~7% porosity.

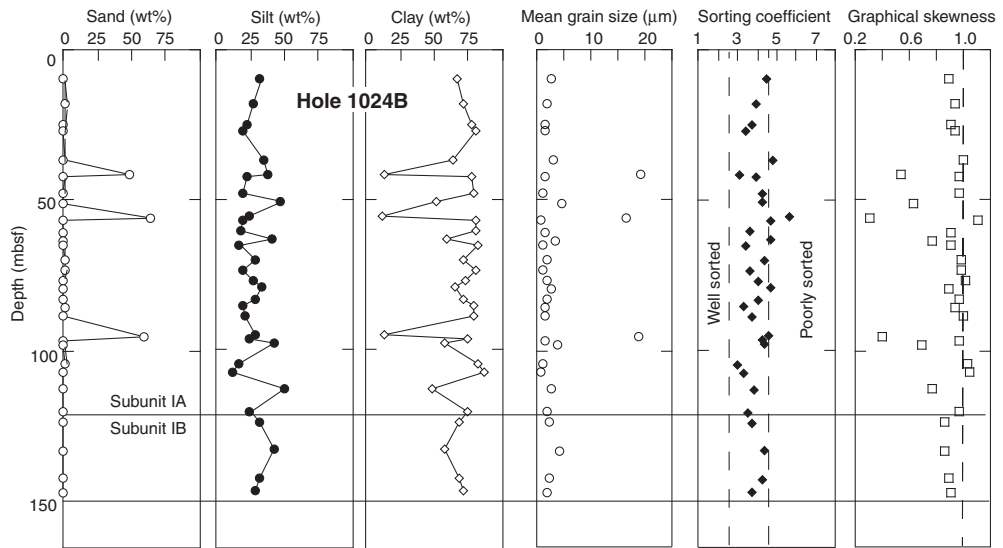


Figure 6. Grain-size profiles for Site 1024.

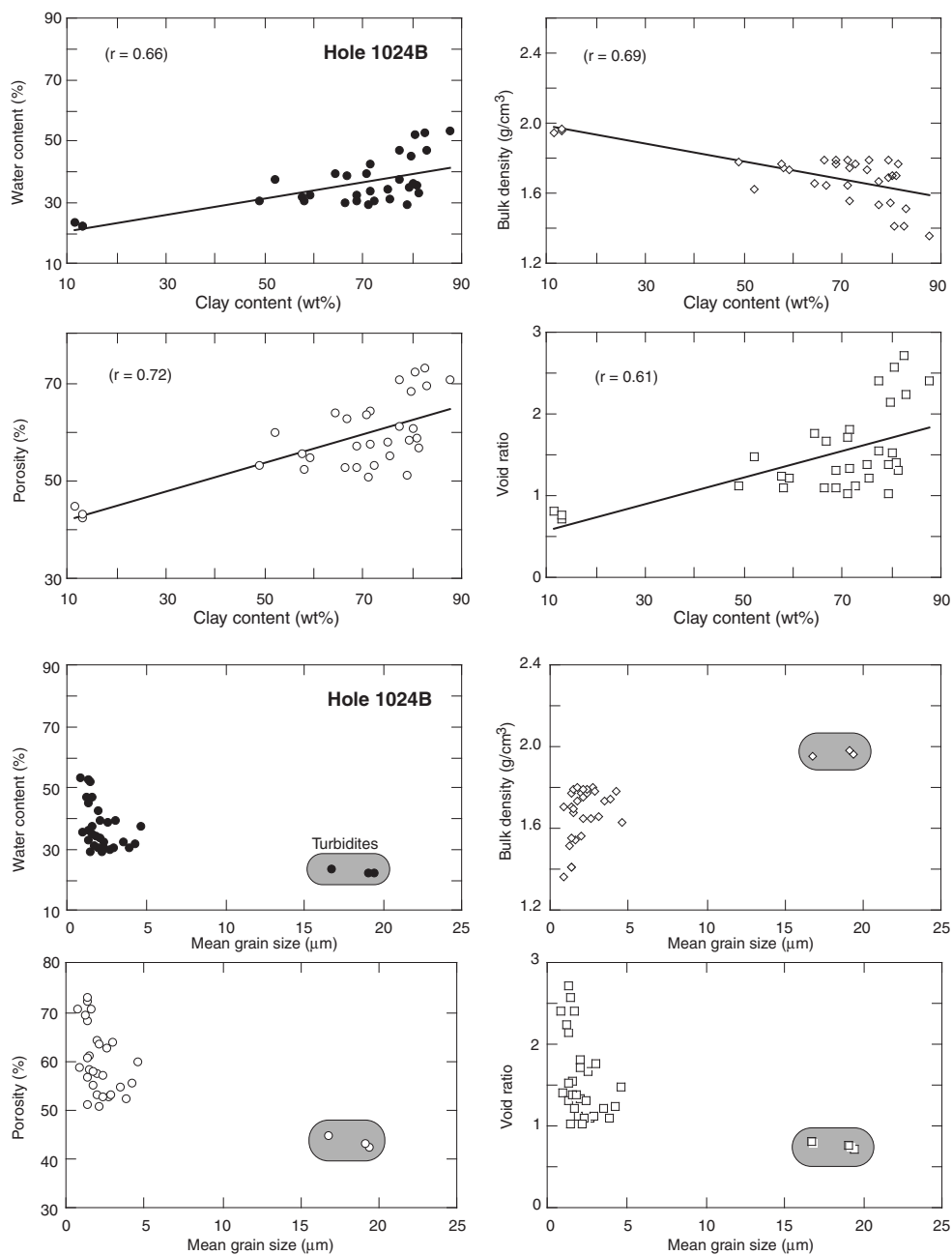


Figure 7. Regression plots for Site 1024.

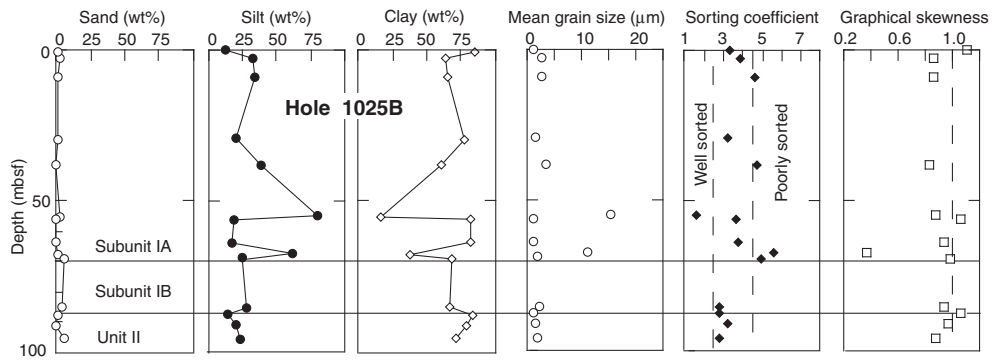


Figure 8. Grain-size profiles for Site 1025.

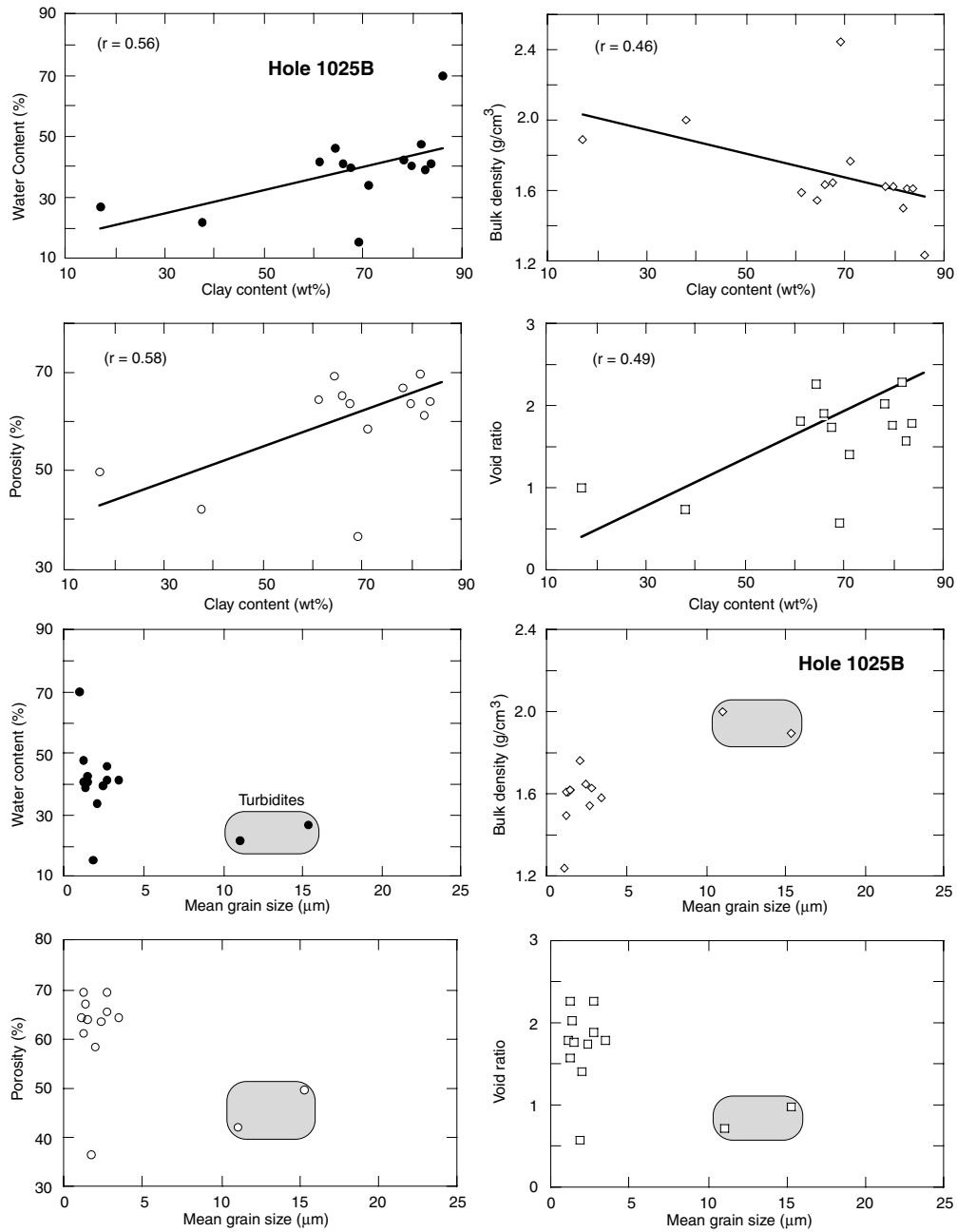


Figure 9. Regression plots for Site 1025.

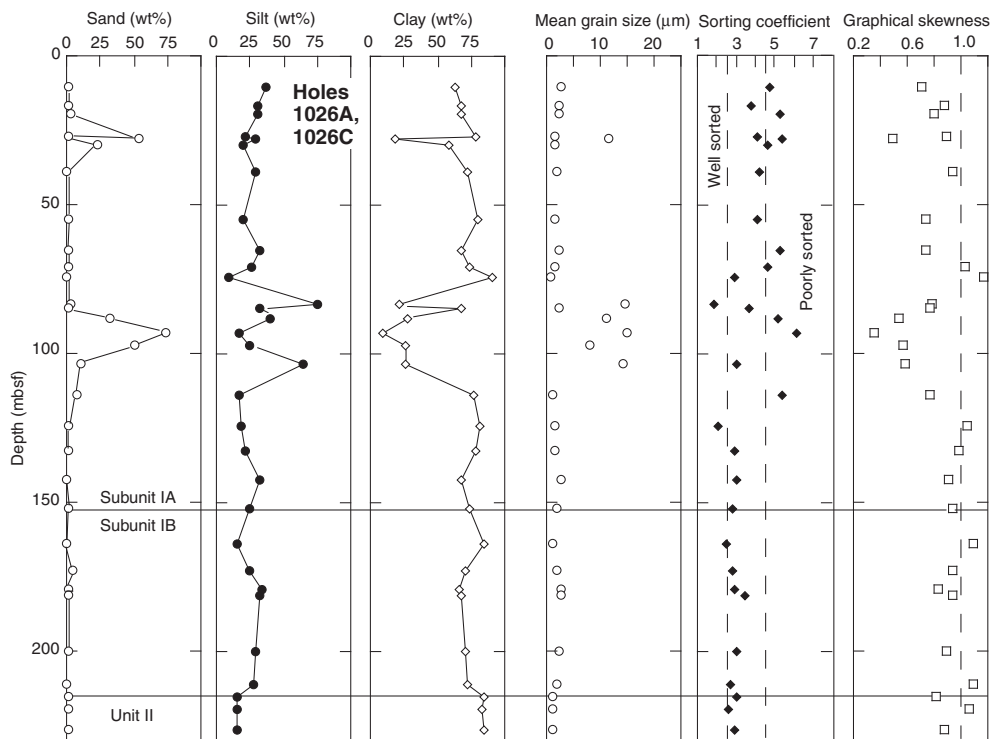


Figure 10. Grain-size profiles for Site 1026.

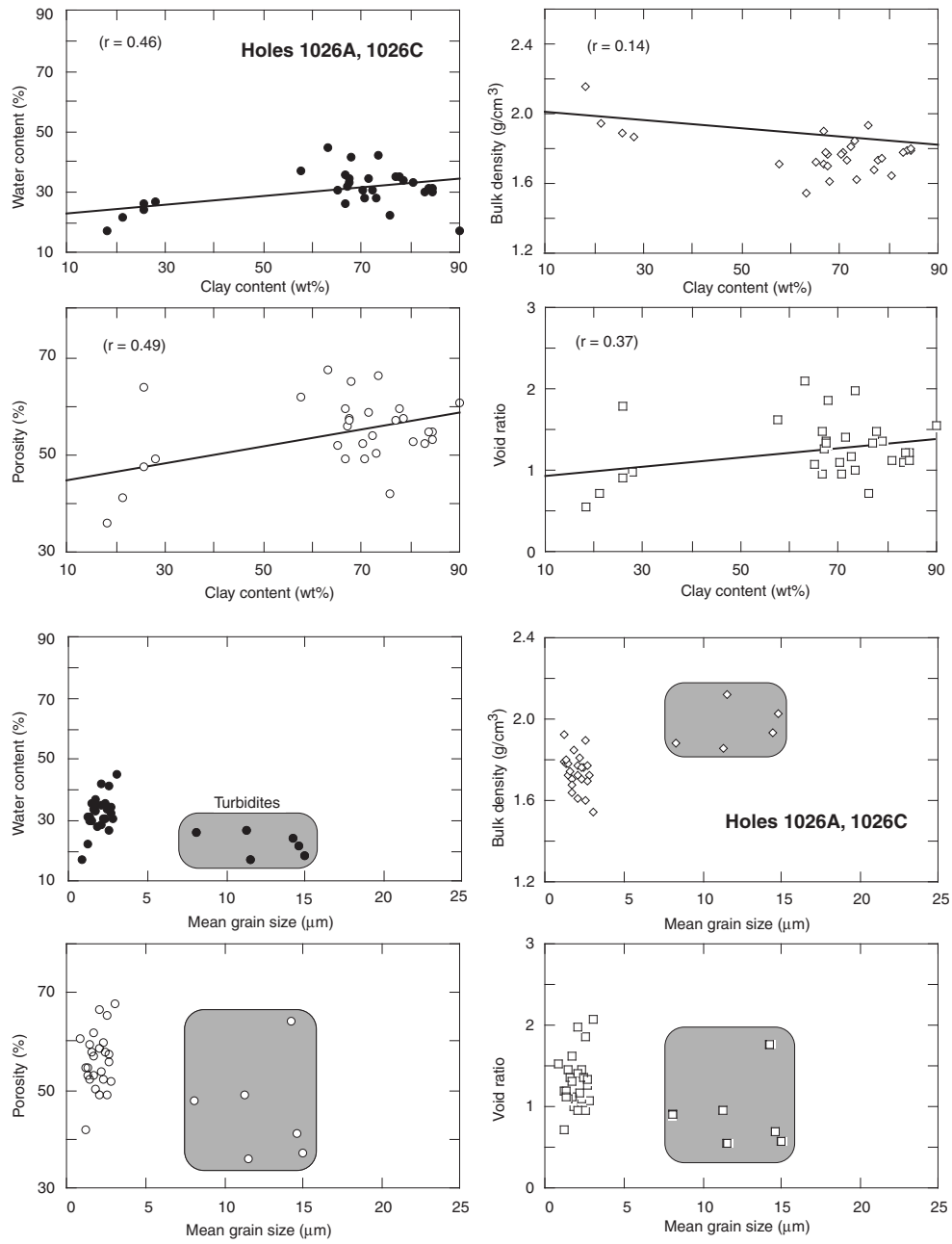


Figure 11. Regression plots for Site 1026.

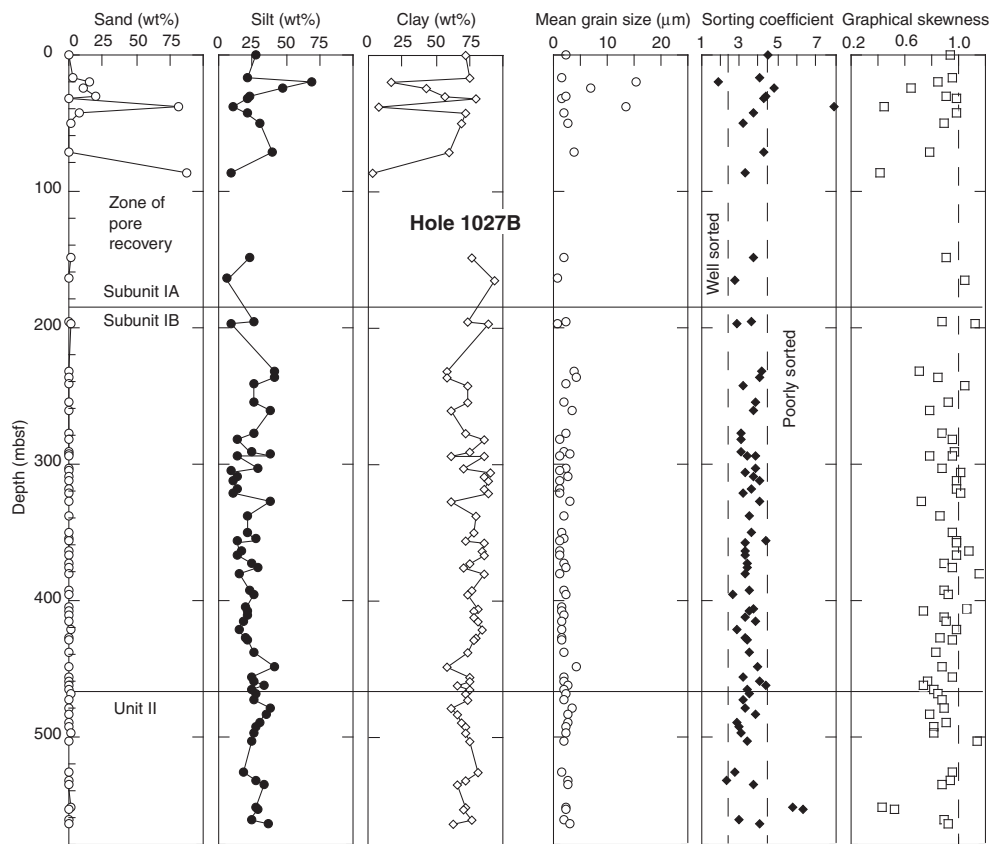


Figure 12. Grain-size profiles for Site 1027.

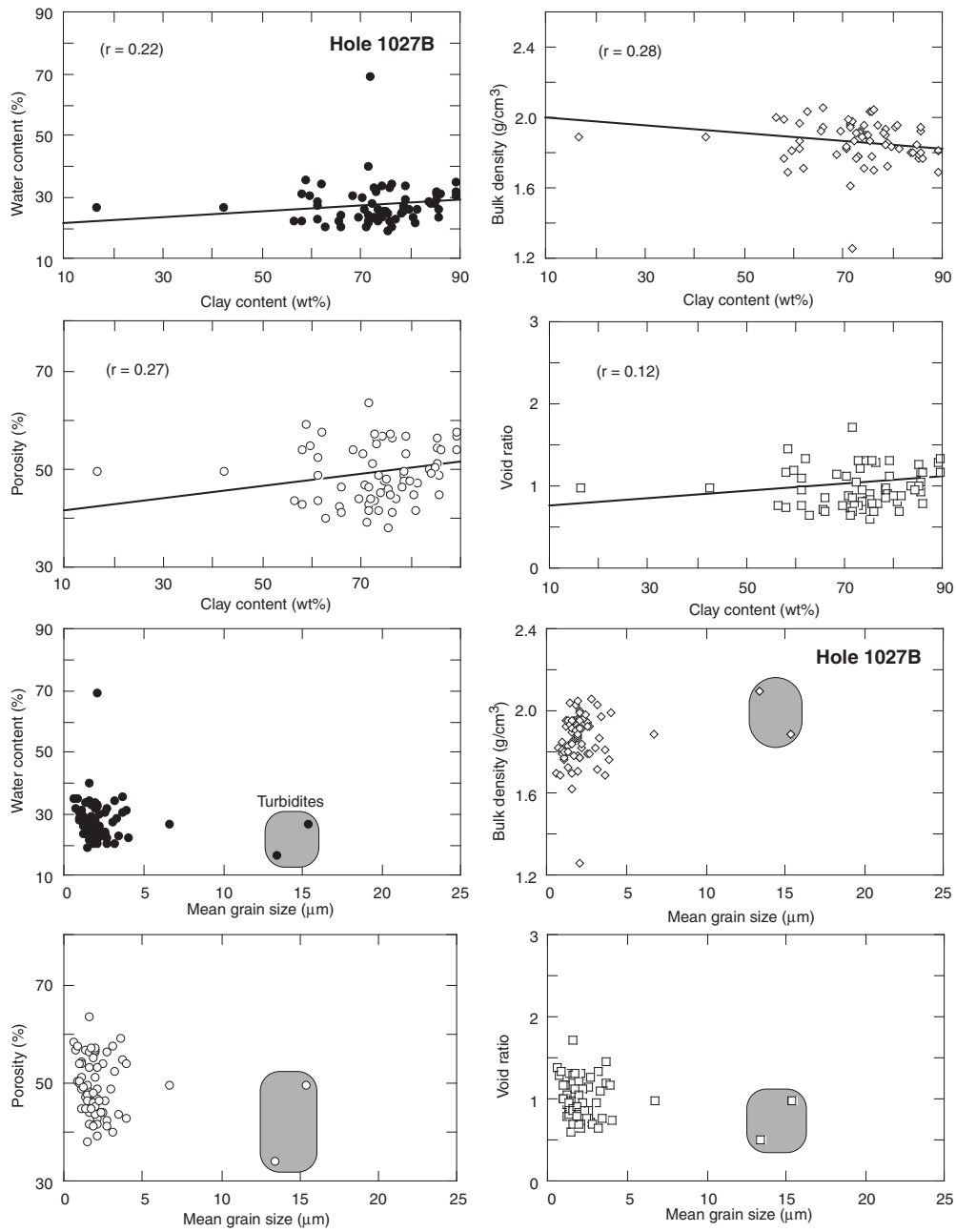


Figure 13. Regression plots for Site 1027.

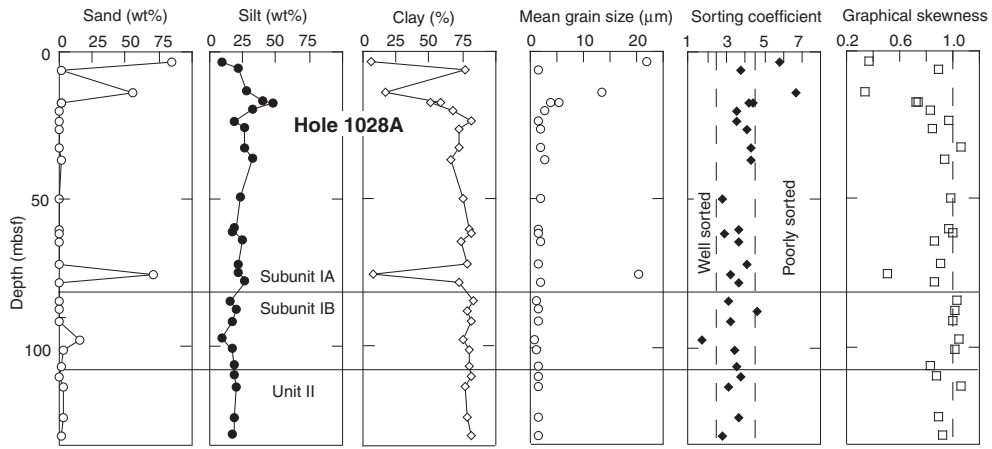


Figure 14. Grain-size profiles for Site 1028.

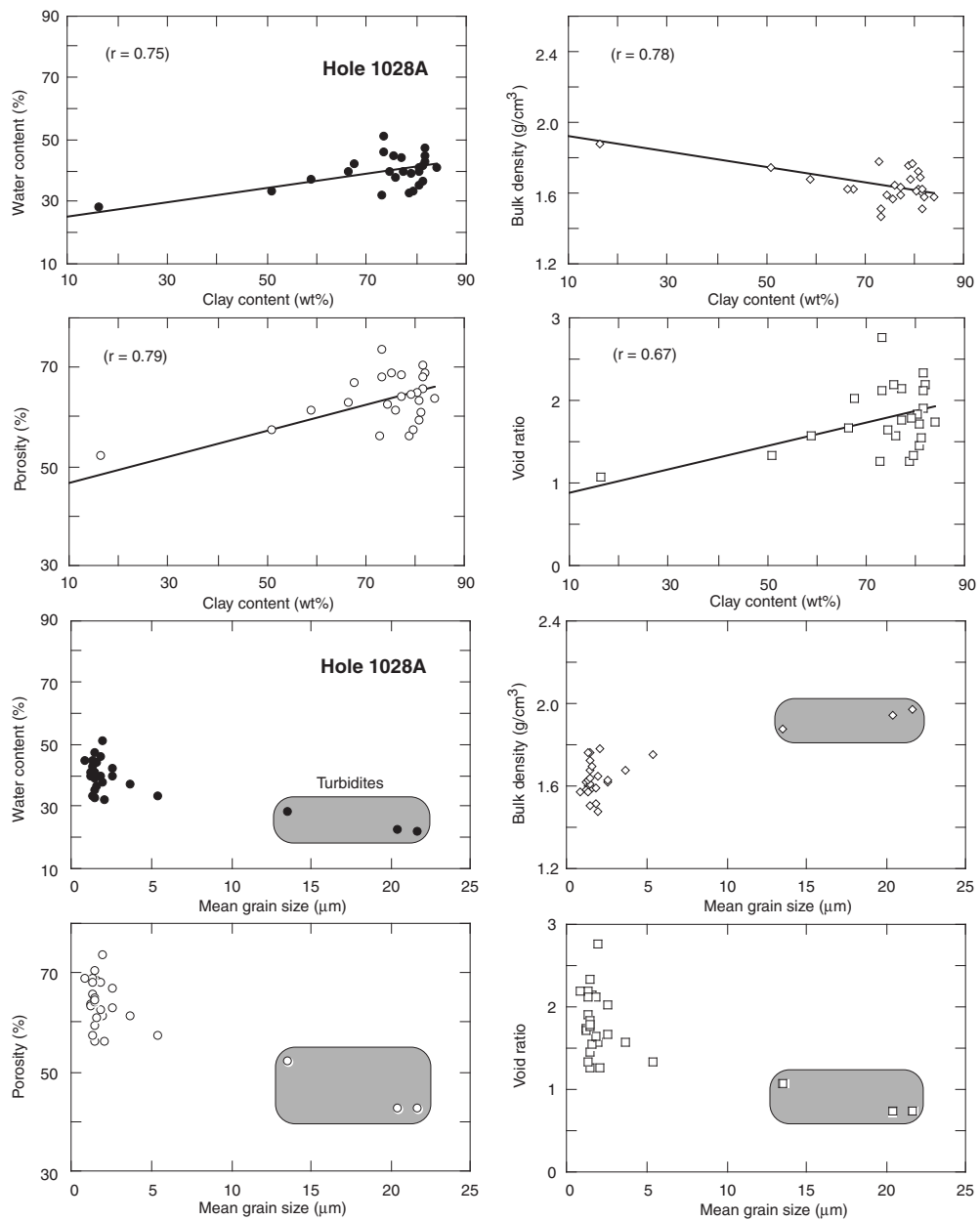


Figure 15. Regression plots for Site 1028.

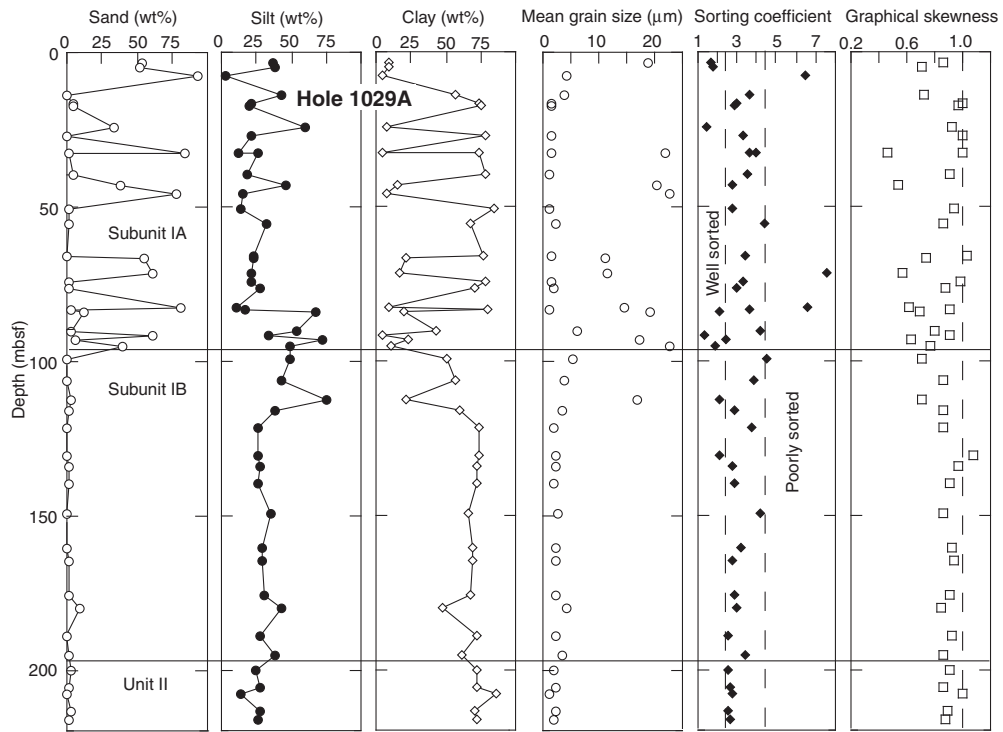


Figure 16. Grain-size profiles for Site 1029.

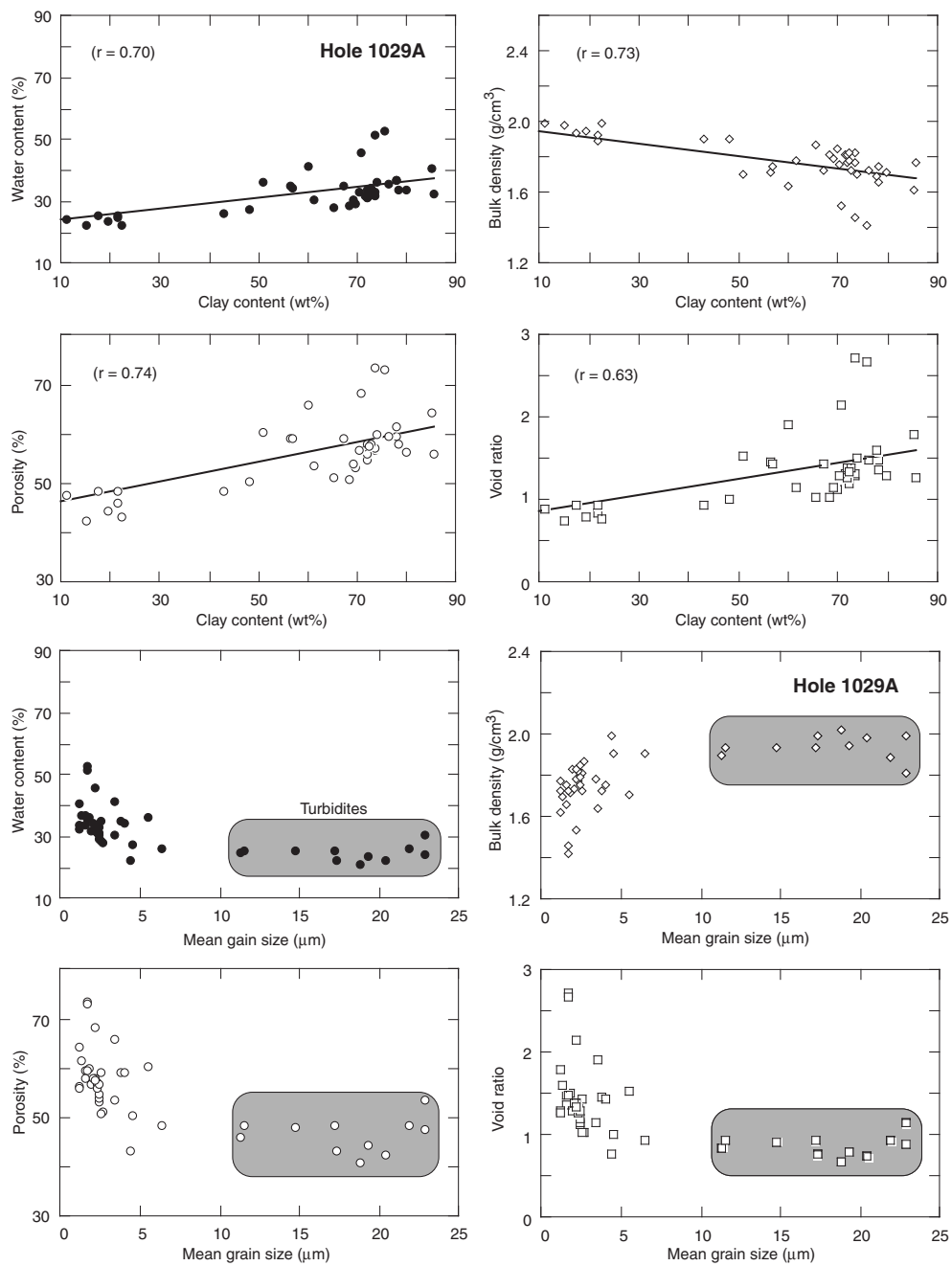


Figure 17. Regression plots for Site 1029.

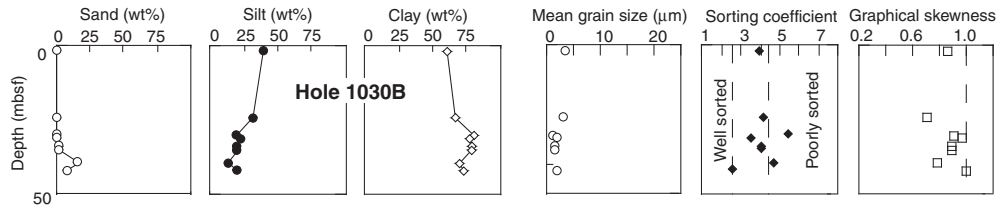


Figure 18. Grain-size profiles for Site 1030.

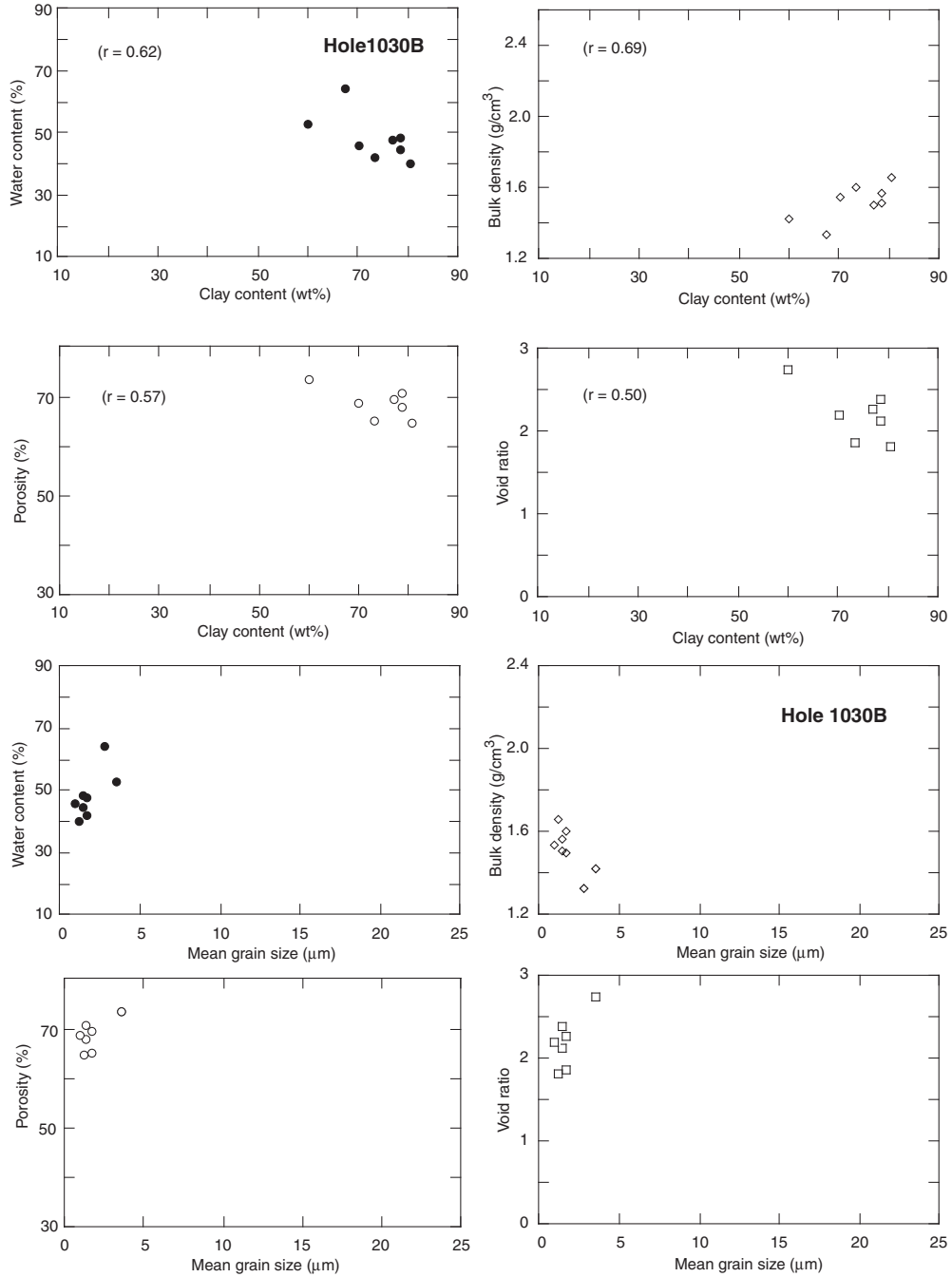


Figure 19. Regression plots for Site 1030.

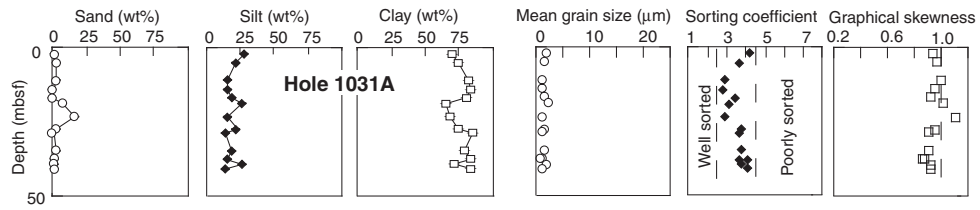


Figure 20. Grain-size profiles for Site 1031.

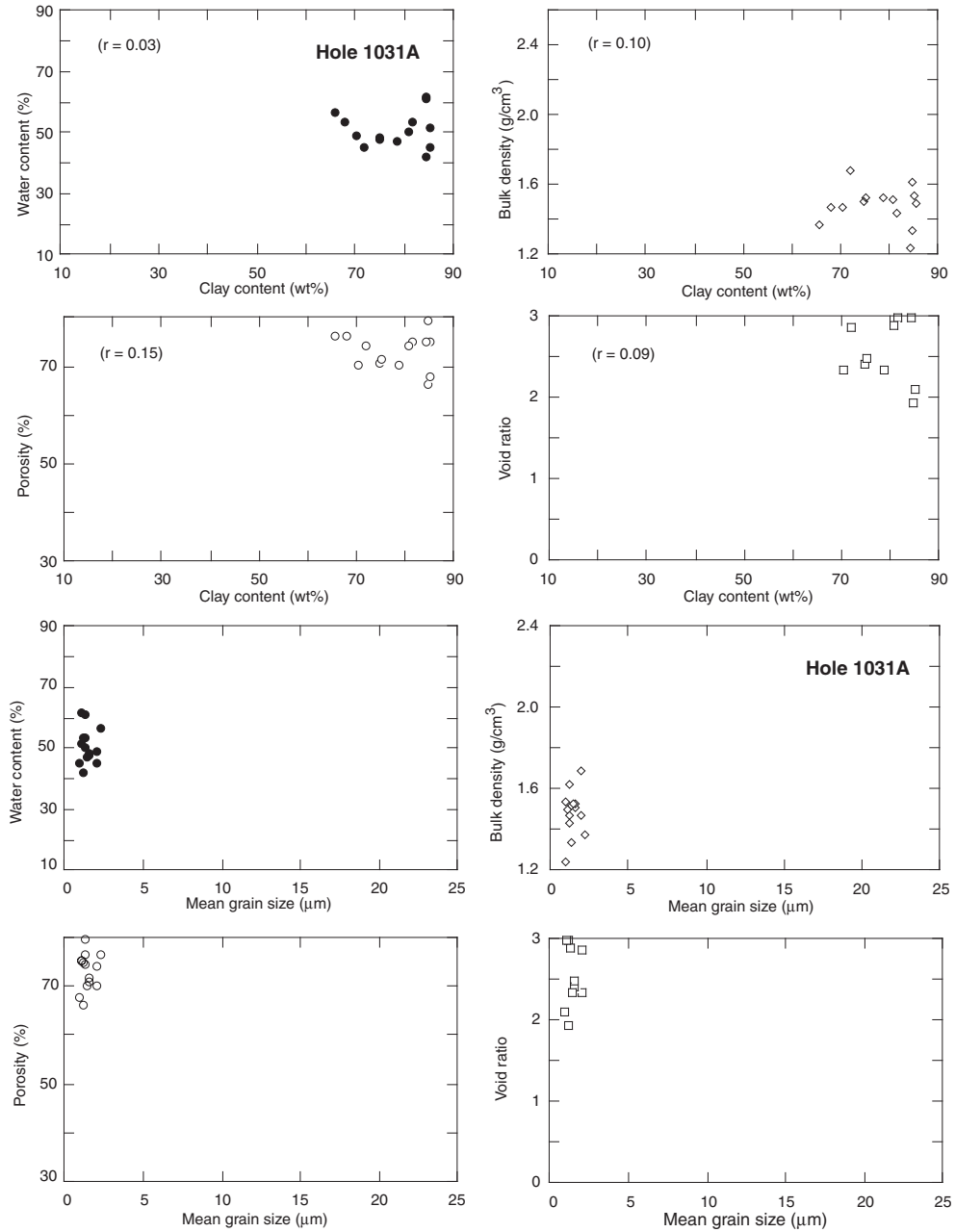


Figure 21. Regression plots for Site 1031.